Observations of Seven Atmospheric Density Current Fronts in Dixon, California*

SHANE D. MAYOR

California State University, Chico, Chico, California

ABSTRACT

Seven atmospheric density current fronts are identified in sequences of ground-based, scanning aerosol backscatter lidar images and in situ micrometeorological time series data that were collected simultaneously and nearly continuously between 15 March and 11 June of 2007 in Dixon, California. The fronts, observed on different days, had the following features in common: 1) an increase in aerosol backscatter intensity, 2) a decrease in air temperature, 3) an increase in water vapor mixing ratio, 4) movement toward the north, 5) airflow from the south in the denser air mass, and 6) occurrence within a 3.5-h time span in the afternoon. The observations support the hypothesis that the fronts are the leading edges of shallow marine air masses advancing northward from the Sacramento–San Joaquin River Delta. The observations are used to test an empirical relationship between front speed, airmass density difference, depth of the dense air mass, and speed of the opposing flow. Prominent features of the fronts such as lobe and cleft structure, billows, and nose and head structure are described. Time-lapse animations of the lidar scans are available in the online version of this article.

1. Introduction

Sea-breeze circulations are long known, often observed and modeled, and the fluid mechanics driving them generally regarded as well understood (Miller et al. 2003; Simpson 1994, 1997; Antonelli and Rotunno 2007; Arritt 1993). Sea-breeze *fronts*, however, are less so perhaps because of the challenge of detecting and observing them and the likelihood that they are less common than the larger-scale circulations of which they are a part. For example, a sea-breeze circulation may exist but not have a well-defined front (Linden and Simpson 1986; Banta et al. 1993). Examples of theoretical and modeling studies of sea-breeze fronts include Benjamin (1968), Pearson (1973), Seitter (1986), and Cunningham (2007). Examples of previous observational research on sea-breeze fronts include Atlas (1960), Eastwood and Rider (1961), Simpson et al. (1977), Kolev et al. (1998), Nakane and Sasano (1986), Lapworth (2000), and Wood et al. (1999). The observations presented here are unique because 1) they include both in situ and scanning lidar data, 2) the lidar images reveal the microscale structure and motion of the fronts on horizontal and vertical cross sections, and 3) the dataset contains 7 fronts out of the nearly-continuous 77 days of data available.

The Raman-shifted Eye-safe Aerosol lidar (REAL; Mayor et al. 2007) was deployed in Dixon, California, between 15 March and 11 June 2007 as an appendix to the Canopy Horizontal Array Turbulence Study (CHATS; Patton et al. 2011). Table 1 lists the specifications of the lidar at the time of the deployment. The primary objective of deploying REAL at CHATS was to test the lidar's ability to detect turbulent coherent structures in the atmospheric surface layer just above a forest canopy. Secondary objectives included monitoring the boundary layer depth and structure of the lower atmosphere that the in situ measurements were embedded within. The REAL was located 1.61 km north (38°30′8″N, 121°50′43″W) of the National Center for Atmospheric Research (NCAR) Integrated Surface Flux Facility (ISFF) 30-m vertical tower (VT).[1] The density current fronts reported here

---

Corresponding author address: Shane D. Mayor, Department of Physics, California State University, Chico, 400 West First St., Chico, CA 95929.
E-mail: sdmayor@csuchico.edu

---

[1] The vertical tower at CHATS was located approximately 100 m north of the structure that supported horizontal arrays of in situ sensors.

TABLE 1. Specifications of the lidar system.

Wavelength	1.543 microns
Pulse energy	170 mJ
Pulse rate	10 Hz
Pulse duration	6 ns
Beam diameter at lidar	66 mm ($1/e^2$ points)
Beam divergence	0.24 mrad (full angle)
Telescope diameter	40 cm
Receiver FOV	0.54 mrad (full angle)
Digitizer speed	100 megasamples per second (MSPS)
Digitizer range	14 bits
Detector type	200-μm InGaAs APD

were an unexpected discovery resulting from the experiment.

The lidar provides two-dimensional images that reveal the horizontal and vertical spatial structure of the clear air via aerosol backscattering. These images reveal the location of the fronts and depths of the boundary layers. By following the location of a front in a series of images, the speed of a front can be obtained. The lidar images and animations also provide convincing evidence of density current fronts advecting over the tower site. Identifying the front passages from the in situ data alone would have been challenging and likely insufficient evidence to prove the existence of a density current front. The in situ data reveal the changes in specific airmass properties such as temperature, relative humidity (RH), and quantities, such as fluxes, that are not possible to obtain from the lidar data.

The lidar scan strategy was periodically changed during CHATS. A scan strategy is composed of some repeating sequence of vertical and near-horizontal scans and brief near-horizontal stares. Vertical scans are referred to as range–height indicator (RHI) and near-horizontal scans are referred to as plan position indicator (PPI). All RHI scans were collected while looking toward 180° azimuth (south). This places the lidar's laser beam just meters west of the ISFF VT. All PPI scans were collected at approximately 0.2° elevation. Therefore, the RHI scans are north–south-oriented vertical cross sections and the PPI scans are almost-horizontal cross sections in the atmospheric surface layer. During a PPI scan at 0.2° elevation, the laser beam intersected the ISFF VT at a 1.6-km range at approximately 12 m AGL. The laser beam was not higher than about 30 m AGL at a 5-km range. The laser beam diameter is estimated to be approximately 45 cm at 1.6-km range and about 1.26 m at a 5-km range.

Dixon, California, is located in Solano County in the central valley of California approximately 100 km east of the Pacific Ocean (see Fig. 1). The terrain near the experimental site is very flat and ranges only between approximately 20 and 30 m MSL within 5 km of the

lidar site. The nearest significant terrain is the North Coast Range approximately 20 km west of the site with peaks of 600 m ASL. The experimental site is also located approximately 20 km north of the Sacramento–San Joaquin River Delta—a large inverted river delta. Dixon and the river delta region are blocked from direct influence of the Pacific Ocean by the South and North Coast mountain ranges, with the exception of a gap at the Carquinez Strait connecting the Delta and the San Francisco Bay. The gap at Carquinez Strait enables the transport of low-altitude air between the San Francisco Bay region and the central valley. Surface airflow diagrams in works by Hayes et al. (1984) and Zaremba and Carroll (1999) indicate how marine air can enter the central valley through the Carquinez Strait and spread into the central valley. The observations presented here support the hypothesis that the fronts are likely to be the leading edges of shallow air masses influenced by the marine environments of the Delta region and possibly the San Francisco Bay and Pacific Ocean.

2. The seven cases

Table 2 lists the dates and times of the seven cases and key quantities determined from the observations. The CHATS dataset contains 77 days of nearly continuous data, and the cases were identified by inspecting both lidar images and time series traces of in situ variables for steplike changes.[2] Although synoptic and regional weather analyses for the cases have not yet been performed, the lidar and in situ data described below indicate that they all occurred in cloud-free environments and during fair-weather conditions.

a. 15 March 2007

This case occurred on the first day of the CHATS experiment and the in situ measurements were not yet being collected. Therefore, only lidar data exist for this case. Figure 2 shows one PPI scan (left panel) and one RHI scan (right panel) of the front. (A time-lapse animation of the scans in the form of an MPEG movie is available as supplemental material at the Journals Online Web site: http://dx.doi.org/10.1175/2010MWR3374.s1.) The lidar was collecting temporally interleaved PPI and RHI scans for the full duration of this event. PPI scans were collected between 151.4° and 211° azimuth at 0.2° elevation. RHI scans were collected between 0.43° and 34.6° elevation at 181° azimuth. The scan rate was 4° s^{-1} in both types of scans. Therefore, the PPI required 15 s and

---

[2] Evidence of the fronts does not appear in sodar-radio acoustic sounding system (RASS) observations that were collected nearby.
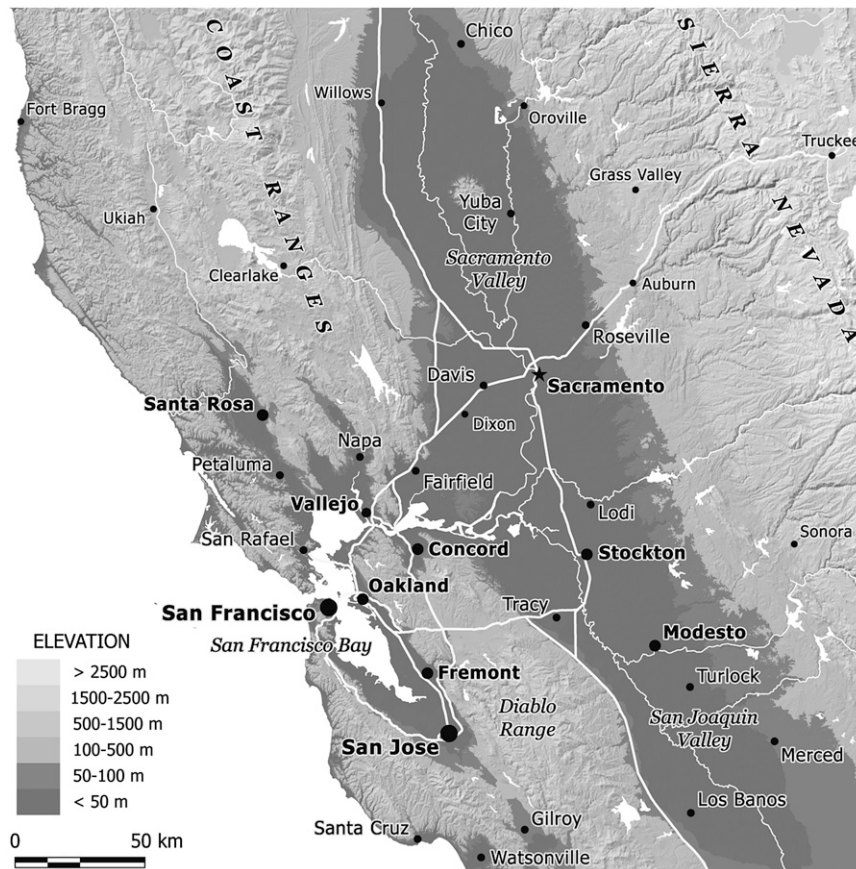
FIG. 1. Shaded relief map of the central California region. The observations presented were collected in Dixon that is located near the center of the map.

the RHI required 9 s to collect. Aerosol backscatter data were recorded in 1.5-m increments to a maximum range of 10.7 km.

The front becomes apparent in the lidar scans between the 7- and 9-km range and between 2340 and 2352 UTC. It arrives at the ISFF VT at approximately 0050 UTC (1650 PST). Therefore, the average northerly velocity component of the front during the hour before it reached the VT was approximately 1.5 m s^{-1}. RHI scans made prior to the arrival of the front (shown in animation) reveal plumes, or large eddies, that reach up to altitudes of about 800 m AGL (the outer boundary layer depth). [3] A strong aerosol backscatter gradient exists between 1000 and 1200 m AGL, but plume structures are not observed within it. The lidar animation shows aerosol plumes moving to the south (indicative of northerly airflow) in the less dense air mass (the outer boundary layer) and aerosol features moving to the north in the more dense air mass

(the marine layer or internal boundary layer) indicative of southerly flow behind the front. The animation shows that the outer ML depth decreases slightly during the passage of the front. The outer ML depth and an aerosol layer at approximately 1500 m AGL reveal a wavelike undulation with an amplitude of about 200 m as the front

TABLE 2. Dates and times of the density current fronts observed during CHATS and the corresponding changes in air temperature, water vapor mixing ratio, relative humidity, aerosol backscatter intensity, and the northerly component of front speed. Times listed are when the front passed over the ISFF VT site. The changes in airmass properties were obtained by averaging the data for 30 min before and after passage of the front.

Date (2007)	Time (UTC)	ΔT (°C)	Δm (g kg^{-1})	ΔRH (%)	ΔdB	V_{front} (m s^{-1})
15 Mar	0050	—	—	—	1.9	1.5
24 Apr	0037	−0.94	1.62	11.8	3.0	3.0
26 Apr	0101	−1.52	2.19	11.7	2.7	2.0
1 May	0100	−1.54	2.40	13.4	5.0	1.0
14 May	2313	−0.45	1.86	7.6	1.0	1.3
28 May	2248	−0.60	1.60	6.8	2.2	1.1
10 Jun	2139	−0.86	2.52	11.9	6.0	3.8

---

[3] Outer boundary layer or outer mixed layer (ML) refers to the deeper and less dense air mass.
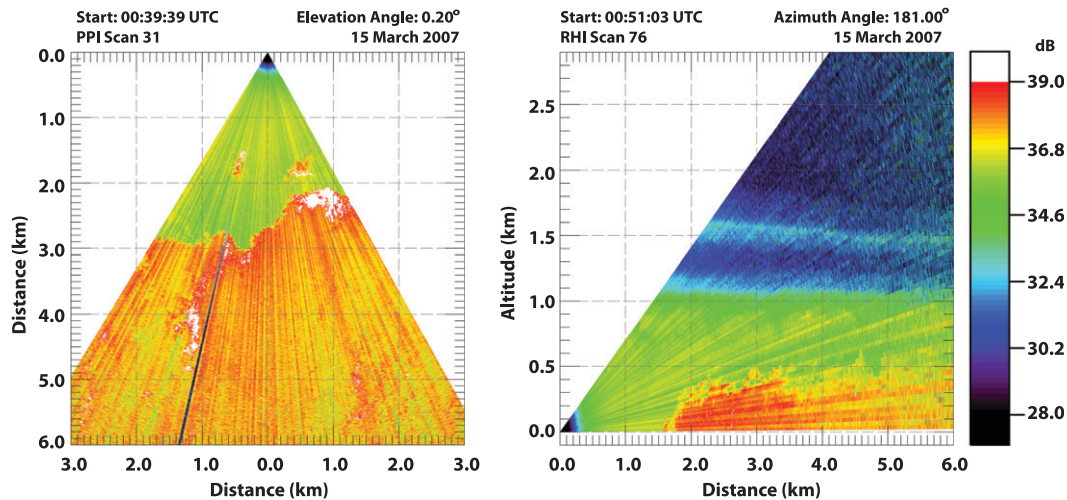
FIG. 2. (left) PPI and (right) tall RHI scans from 15 Mar 2007. Note the vertical axis in (right) is expanded by a factor of 2 relative to the horizontal axis.

passes beneath. A similar dip is observed in the 26 April and 10 June cases and is consistent with that shown in diagrams in previous publications including Fig. 23 in Simpson et al. (1977). In fact, the outer layer rises by about 100 m as the leading edge of the front passes beneath. This wave structure is most pronounced in the RHI frame from 0042:28 UTC. Also, one aerosol plume emanating from the surface at the 3-km range at 0021 UTC ascends over the leading edge of the front. The advancing marine layer behind the head of the front remains below 500 m AGL. The PPI animation reveals that the eastern portion of the front surges northward more rapidly than the western portion as it approaches the lidar site. Examination of the lidar backscatter from a single pulse directed horizontally through the front indicates that the relative aerosol backscatter intensity increased by approximately 1.9 dB (from 36 to 37.9 dB) within several tens of meters. This is equivalent to a 54% increase in the backscatter intensity.

b. 24 April 2007

During this case, the lidar was programmed to repeat a series of *wide* and *narrow* PPI scans, *tall* and *shallow* RHI scans, and a horizontal stare. The purpose of the scan strategy was to obtain high angular and temporal resolution lidar data close to the ISFF towers in search of turbulent coherent structures part of the time, while capturing the structure and motion of the larger scales, including boundary layer depth, at other times. In this case, and all of the following cases, the lidar was programmed to record backscatter to a maximum range of 5.8 km instead of 10.7 km as in the previous case. The lidar was collecting narrow PPI scans at the time the

front arrived at the ISFF VT (0037 UTC). At 0018 UTC, the front was located approximately 5 km south of the lidar site (3.4 km south of the ISFF VT). Based on the images, the northerly component of forward front speed is approximately 3 m s^{-1}. Pairs of tall RHI scans, necessary to reveal the full vertical extent of the front, were collected at 0009, 0017, 0029, and 0039 UTC. These frames reveal billows of the advancing marine air mass reaching as high as 1 km AGL. Figure 3 shows a wide PPI and a tall RHI scan of the front. (A time-lapse animation of the scans in the form of an MPEG movie is available as supplemental material at the Journals Online Web site: http://dx.doi.org/10.1175/2010MWR3374.s2.)

Of the 6 cases for which in situ data are available, this front was the coldest on both sides. The average temperature on each side of the front ($\pm$30 min of front passage) was 6°–8°C colder than the other cases. Temperature sensor data from the ISFF VT show the air temperature decreased by approximately 1°C during the 1-h period surrounding this front passage (see Fig. 4a). The average temperature in the 30 min before 0037 UTC was 22.75°C with a maximum of approximately 23.15°C and in the 30 min after averaged 21.81°C with a minimum of 21.5°C. During the same period the mean water vapor mixing ratio increased from an average of 5.60 g kg^{-1} before the front to 7.21 g kg^{-1} after the front (see Fig. 5a). These changes resulted in an increase in the mean relative humidity from 32% to 44%. Surface barometric pressure was almost constant during the 1-h period at 1016.3 hPa.[4] The lidar backscatter data indicate that the

---

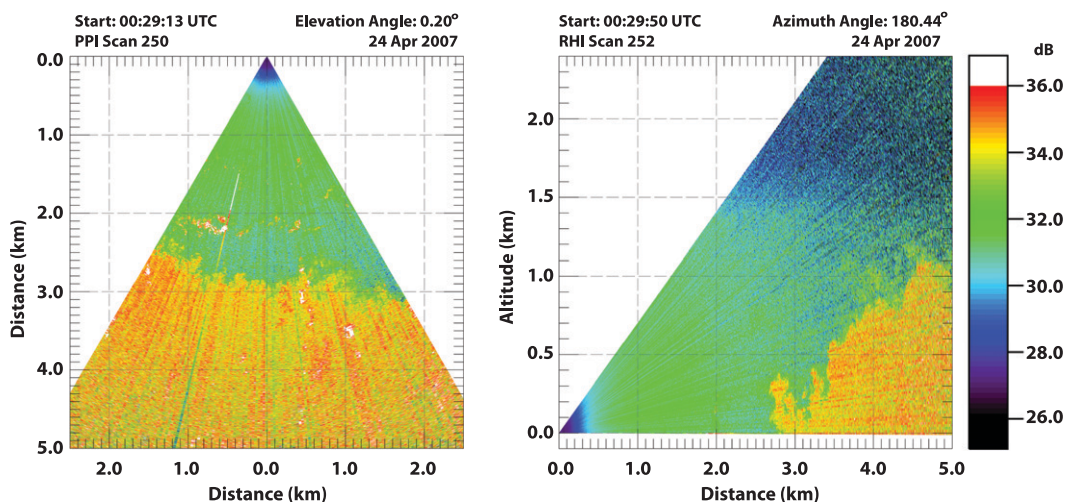[4] The barometer recorded pressure to the nearest 0.1 hPa at 1 Hz.

FIG. 3. (left) PPI and (right) RHI scans from 24 Apr 2007. Note the vertical axis in (right) is expanded by a factor of 2 relative to the horizontal axis.

relative aerosol backscatter intensity increased by approximately 3 dB (from 31.5 to 34.5 dB). This is equivalent to a doubling in backscatter intensity. Average wind speeds increased from about 1.65 m s^{-1} before the front to 2.65 m s^{-1} after the front. The in situ data show no significant shift in the wind direction.

In situ temperature, relative humidity, and pressure data were used to calculate moist air density for the 1-h periods surrounding front passages (see Fig. 6). The appendix describes the steps used to calculate water vapor mixing ratio and moist air density. In the case of 24 April, the 30-min average moist air density increased from 1.192 53 to 1.195 19 kg m^{-3}—a 0.22% increase (Fig. 6a). The dashed horizontal lines in Figs. 4–6 represent the 30-min averages before and after front passage.

c. 26 April 2007

The scan strategy used in this case was identical to that used in the 15 March case. Figure 7 shows a wide PPI scan and a tall RHI scan of the front. (A time-lapse animation of the scans in the form of an MPEG movie is available as supplemental material at the Journals Online Web site: http://dx.doi.org/10.1175/2010MWR3374.s3.) RHI scans show the mixed layer over the study area and north of the front to have a deep entrainment zone relative to the average mixed layer depth of approximately 1 km. The RHI scans in the animation of this case reveal plumes of the air mass north of the front reaching altitudes as high as approximately 1500 m AGL as the front and marine air mass move into the range of the lidar. The RHI scans show billows of the marine airmass reaching as high as 800 m AGL. The RHI scans also reveal an aerosol layer in the stable atmosphere between 2.25 and 2.75 km AGL and the base of another layer at 3 km AGL before

the front arrives. These layers decrease in altitude by almost 300 m as the front passes beneath. Scans show the front located at the 5-km range at 2256 UTC and reaching the ISFF site at 2325 UTC. Therefore, the northern component of movement was 1.95 m s^{-1}.

Of the six cases for which in situ data are available, this case had the largest and sharpest decrease in air temperature with the front passage (Fig. 4b). The average air temperature during the 30 min before the arrival of this front was 28.65°C and dropped to the 30-min postfront average of 27.14°C in about 6 min. The mean water vapor mixing ratio increased from 5.44 to 7.63 g kg^{-1} (Fig. 5b). The changes in temperature and water vapor mixing ratio resulted in an 11.7% increase in RH. Average moist air density increased by 0.36% from 1.161 38 to 1.165 59 kg m^{-3} (Fig. 6b). Surface barometric pressure decreased slightly from 1009.5 to 1009.2 hPa during the 1-h period. The relative aerosol backscatter increased by about 2.7 dB with the passage of this front (from 35.8 to 38.5 dB). This is equivalent to a 90% increase in backscatter intensity. The average wind speed increased only slightly from 1.76 to 1.86 m s^{-1}. However, this case had the largest change in wind direction: from 350.5° before the front to 221.1° after the front.

d. 1 May 2007

The most striking characteristic of this front as revealed by the lidar images is the presence of large lobe structures that propagate toward the northeast as the front advances to the north. Breaking and semistationary billow structures can be identified in the RHI scans between 0114 and 0145 UTC. The largest of these have amplitude on the order of 500 m in the vertical and wavelengths of approximately 2 km in the horizontal direction. Figure 8
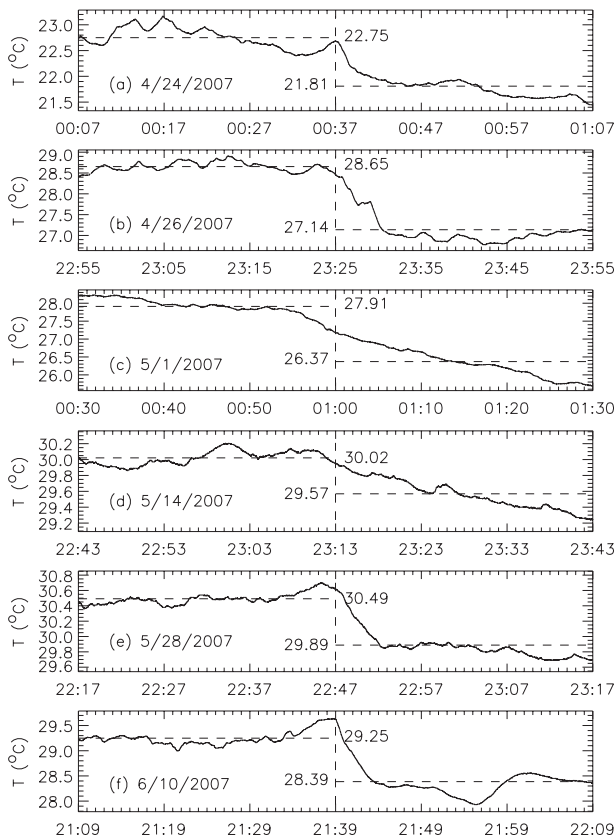
FIG. 4. Temperature at 1 Hz as observed at 10 m AGL on the ISFF VT for the 1-h periods surrounding the front passage. The dashed horizontal lines show the mean values for the 30 min before and after the front passage.
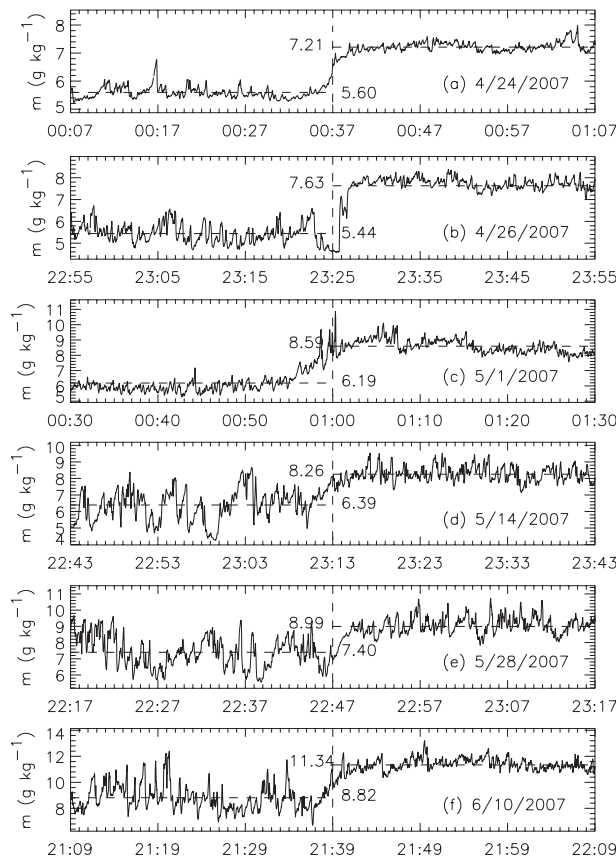

FIG. 5. Water vapor mixing ratio computed from observed temperature, pressure, and relative humidity at 1 Hz and 10 m AGL on the ISFF VT for the 1-h periods surrounding front passage. The dashed horizontal lines show the mean values for the 30 min before and after the front passage.

shows a wide PPI and a tall RHI scan of the front. (A time-lapse animation of the scans in the form of an MPEG movie is available as supplemental material at the Journals Online Web site: http://dx.doi.org/10.1175/2010MWR3374.s4.) The scan strategy used in this case is the same as in the 15 March and 26 April cases (alternating wide PPI and tall RHI).

The mean air temperature in the 30 min prior to arrival of this front was 27.91°C with a small cooling trend of about 0.5° (30 min)$^{-1}$ (Fig. 4c). After the passage of the front at 0055 UTC the slope of temperature trend steepens to about −2.0°C (30 min)$^{-1}$. The mean water vapor mixing ratio increased from 6.19 to 8.59 g kg^{-1} (Fig. 5c). This resulted in a 13.4% increase in RH. The moist air density increased from 1.161 54 to 1.165 78 kg m^{-3}, a 0.37% change. Surface barometric pressure decreased slightly from 1007.6 to 1007.4 hPa during the 1-h period (Fig. 6c). The relative aerosol backscatter intensity increased approximately 5 dB—equivalent to a 220% increase. Anemometer data show the average wind speed increasing from 1.89 to 2.61 m s^{-1} and the average

wind direction shifting from 255.3° to 202.7° with the passage of the front.

e. 14 May 2007

This front arrived at the ISFF VT site at 2313 UTC. The scan strategy used during this case is the same as in the 15 March, 26 April, and 1 May cases (alternating wide PPI and tall RHI). Figure 9 shows an RHI and a PPI scan of the front. (A time-lapse animation of the scans in the form of an MPEG movie is available as supplemental material at the Journals Online Web site: http://dx.doi.org/10.1175/2010MWR3374.s5.) This case had the smallest change in aerosol backscatter intensity across the front. The average aerosol backscatter north of the front was strong compared to the other cases: about 38.75 dB and between 39 and 40 dB south of the front. The outer mixed layer depth during this front passage is well defined in the lidar data and is approximately 1250 m AGL. Billows associated with the leading edge of the front reach altitudes of 800 m AGL. The
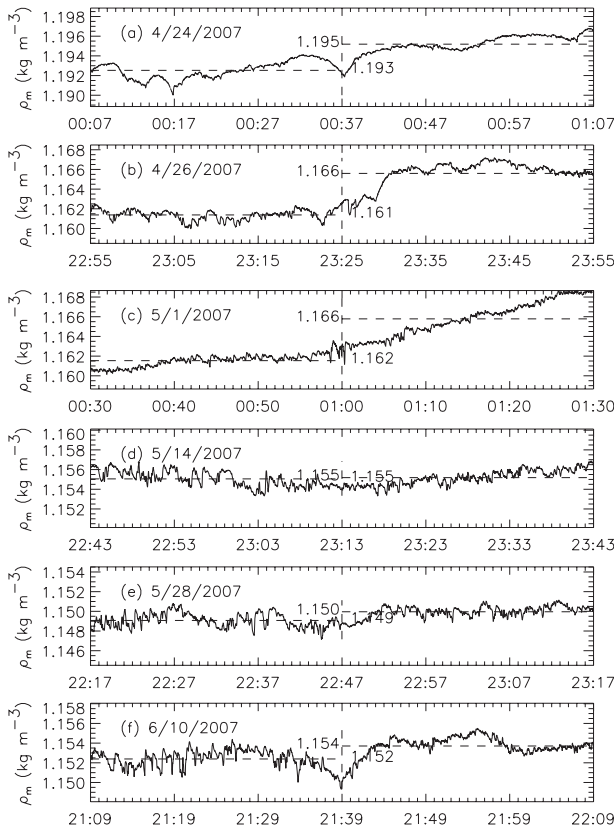
FIG. 6. Moist air density computed from observed temperature, pressure, and relative humidity at 1 Hz and 10 m AGL on the ISFF VT for the 1-h periods surrounding the front passage. The dashed horizontal lines show the mean values for the 30 min before and after the front passage.

mean northerly component of the forward speed of this front was approximately 1.25 m s^{-1} based on it traversing 2400 m in the 32 min prior to its arrival at the ISFF site.

The average air temperature at the ISFF VT during the 30 min before arrival of the front was 30.02°C (see Fig. 4d). A cooling trend begins with the arrival of the front and the air temperature decreases to 29.3°C during the 30 min after front passage. The mean water vapor mixing ratio increased from 6.39 to 8.26 g kg^{-1} (Fig. 5d). These resulted in a 7.6% increase in RH. The mean moist air density increased only slightly by 0.01% from 1.155 05 to 1.155 18 kg m^{-3} (Fig. 6d). Surface barometric pressure decreased slightly from 1009.3 to 1008.7 hPa during the 1-h period. The average wind speed increased from 0.95 to 1.65 m s^{-1} and the average wind direction from 145.5° to 199.5° with the passage of the front.

f. 28 May 2007

For this case, the lidar was programmed to perform a scan sequence similar to that of 24 April, except modified

to collect 80-frame sequences of each type instead of 40 in order to provide longer-duration animations. As a result, the data for this case include a series of wide PPI and a series of short RHI scans of the front with high temporal resolution. Tall RHI scans were collected infrequently. (A time-lapse animation of the wide PPI scans in the form of an MPEG movie is available as supplemental material at the Journals Online Web site: http://dx.doi.org/10.1175/2010MWR3374.s6. A time-lapse animation of the short RHI scans in the form of an MPEG movie is available as supplemental material at the Journals Online Web site: http://dx.doi.org/10.1175/2010MWR3374.s7.) Figure 10 shows a wide PPI and a tall RHI of the front.

The lidar data indicate that the front arrived at the ISFF VT at 2248 UTC. Tall RHI scans at 2222 UTC reveal a broad gradient of aerosol backscatter between 1 and 2 km AGL, but it is not possible to determine the outer boundary layer depth from these images. In these same frames, the front is at the 3.6-km range and plumes reach altitudes of 500–900 m AGL at distances of 1–2 km behind the front. Tall RHI scans collected at 2301 UTC show plumes reaching as high as 1 km AGL and evidence that an entrainment zone exists up to 1.5 km AGL.

The relative aerosol backscatter increased approximately 2.2 dB (from 35.3 to 37.5) in this case corresponding to a 70% increase. The air temperature decreased from an average of about 30.5°C prior to arrival of the front to 29.9°C after the front, a change of −0.6°C (Fig. 4e). The average water vapor mixing ratio increased from 7.40 to 8.26 g kg^{-1} with the passage of the front (Fig. 5e). These resulted in a 6.8% increase in RH. The mean moist air density increased by 0.08% from 1.149 07 to 1.149 96 kg m^{-3} (Fig. 6e). Surface barometric pressure decreased slightly from 1006.1 to 1005.5 hPa during the 1-h period. The average wind direction changed from 117.3° to 178.5° with the passage of this front while the average wind speed increased from 1.09 to 1.80 m s^{-1}. During the 11 min prior to arrival at the ISFF site, the front advanced 1600 m giving it an average speed of 2.4 m s^{-1}. However, during the 36 min prior to arrival, it moved 2400 m, giving it an average speed of 1.1 m s^{-1}. This observation shows the varying nature of the speed of the front.

The last tall RHIs collected before arrival of the front at the ISFF site, indicate that the peak height of the head of the advancing marine air mass reached about 900 m AGL. Tall RHI frames collected after the front moves north of the REAL, show mixing extending above 1 km AGL.

g. 10 June 2007

For this case, the lidar was programmed to scan approximately the same as in the 28 May case. As a result,
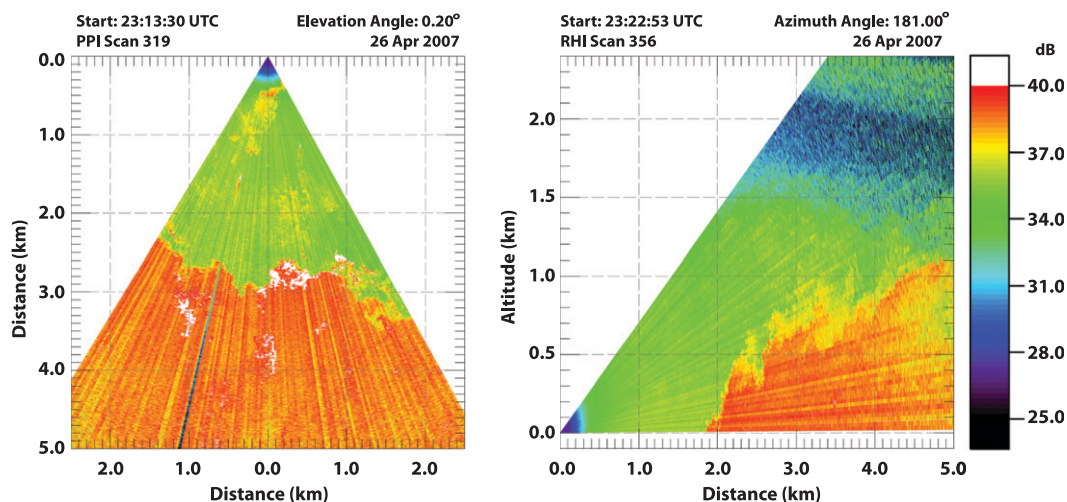
FIG. 7. (left) PPI and (right) RHI scans from 26 Apr 2007. Note the vertical axis in (right) is expanded by a factor of 2 relative to the horizontal axis.

no long sequences of tall RHI scans are available. Tall RHI scans collected before the front arrives at 2055 and 2110 UTC do not show any evidence of an outer mixed layer top. Aerosol backscatter intensity is weak during this period. The first tall RHI scans we have of this front are at 2134 UTC (see right panel in Fig. 11) when the leading edge is approximately 2.5 km from the lidar. The frame shows billows from the advancing marine air mass extending up to altitudes of at least 1 km AGL, possibly 1.5 km AGL. The next tall RHI scans do not occur until 2153 UTC and after the front has moved north of the lidar site. These frames show an aerosol backscattering gradient at about 2 km AGL and a dip with an amplitude of about 250 m have emerged. In

these frames large eddies clearly extend above 1 km AGL, perhaps as high as 1.5 km AGL.

The front in this last case is the fastest of the seven. It moved from the 5-km range to the 1.6-km range over 900 s, giving it a northerly component of 3.8 m s^{-1}. Wide PPI scans (left panel in Fig. 11) show at least one significant lobe, approximately 1 km wide, protruding. (A time-lapse animation of the PPI scans in the form of an MPEG movie is available as supplemental material at the Journals Online Web site: http://dx.doi.org/10.1175/2010MWR3374.s8.)

This case had the largest increase in relative aerosol backscatter: about 6 dB (from 32 to 38 dB) corresponding to a 300% increase. The air temperature dropped from an average of 29.25°C before the front to 28.39°C
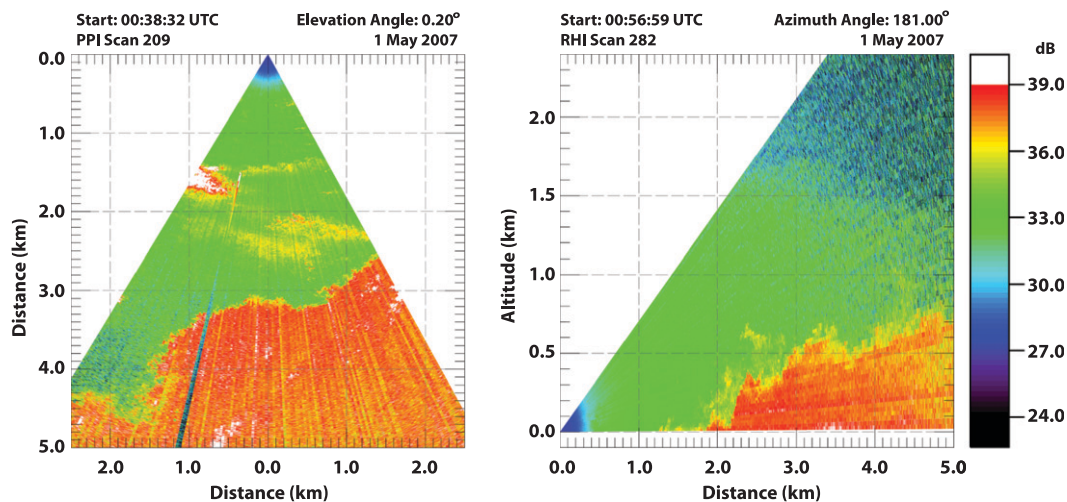

FIG. 8. (left) PPI and (right) RHI scans from 1 May 2007. Note the vertical axis in (right) is expanded by a factor of 2 relative to the horizontal axis.
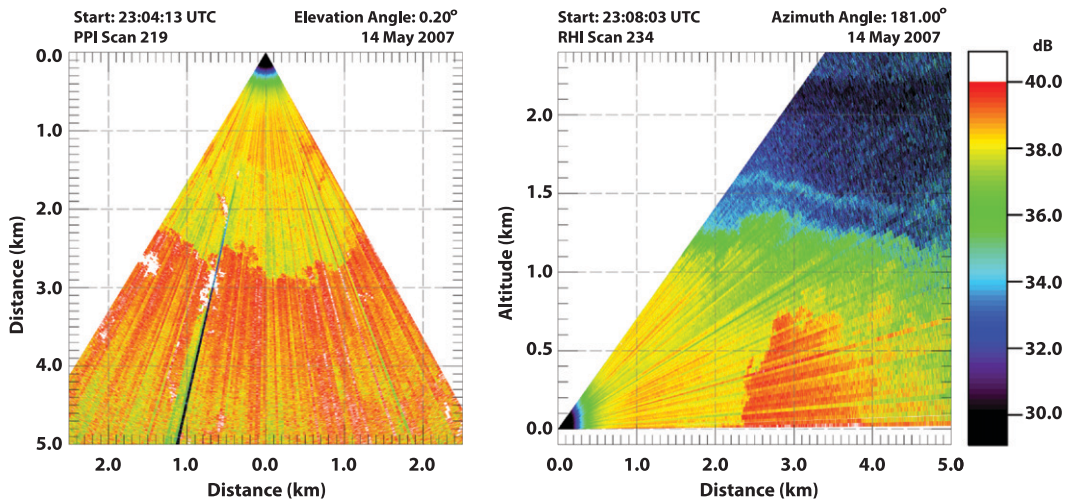
FIG. 9. (left) PPI and (right) RHI scans from 14 May 2007. Note the vertical axis in (right) is expanded by a factor of 2 relative to the horizontal axis.

after the front (Fig. 4f). The mean water vapor mixing ratio increased from 8.82 to 11.34 g kg^{-1} (Fig. 5f). The RH increased by 11.9%. Mean moist air density increased from 1.152 39 to 1.153 71 kg m^{-3}, a 0.11% change (Fig. 6f). Surface barometric pressure decreased slightly from 1005.7 to 1005.2 hPa during the 1-h period. The average wind direction shifted from 264.5° before the front to 203.5° after the front. The 30-min-average wind speed increased the most of the 6 cases: from 1.81 to 3.50 m s^{-1}.

3. Discussion

In all cases for which in situ data are available, time series of temperature (Fig. 4) and water vapor mixing ratio (Fig. 5) show almost steplike changes that correspond with the arrival of the fronts at the ISFF VT. However, pressure data (not shown) do not increase with front passage as one might expect and, in fact, have steadily decreasing trends ranging from 0.2 to 0.6 hPa h^{-1} in 5 of the 6 cases. A pressure increase due to the front may be smaller than the 0.1-hPa resolution of the pressure measurement. The observed reduction in pressure over the 1-h periods may be due to the atmospheric tide that is known to produce a decreasing surface pressure trend in the afternoon in the western United States (Mass et al. 1991).

The time series of moist air density are less consistent (Fig. 6). The 24 April and 10 June cases show a local minimum precisely at the time the front passes over the
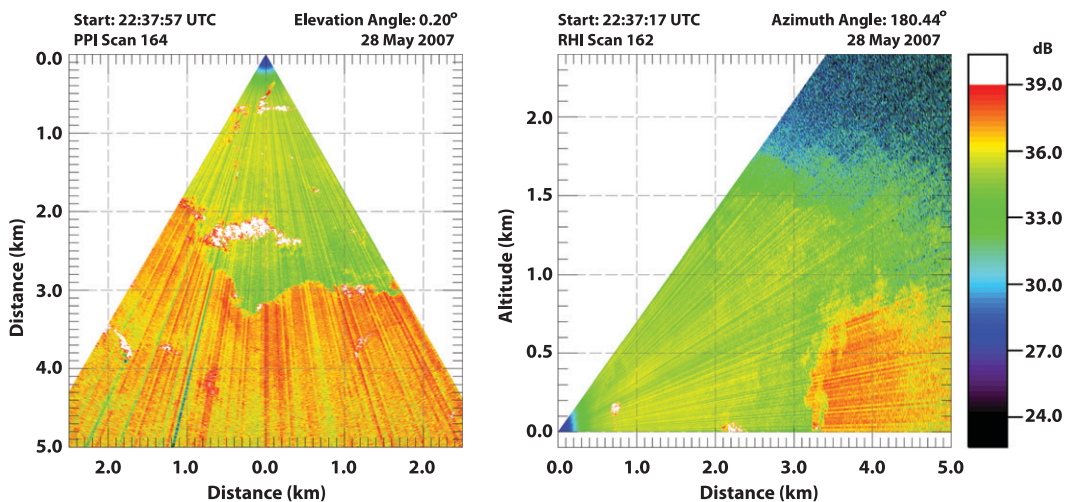

FIG. 10. (left) PPI and (right) RHI scans from 28 May 2007. Note the vertical axis in (right) is expanded by a factor of 2 relative to the horizontal axis.
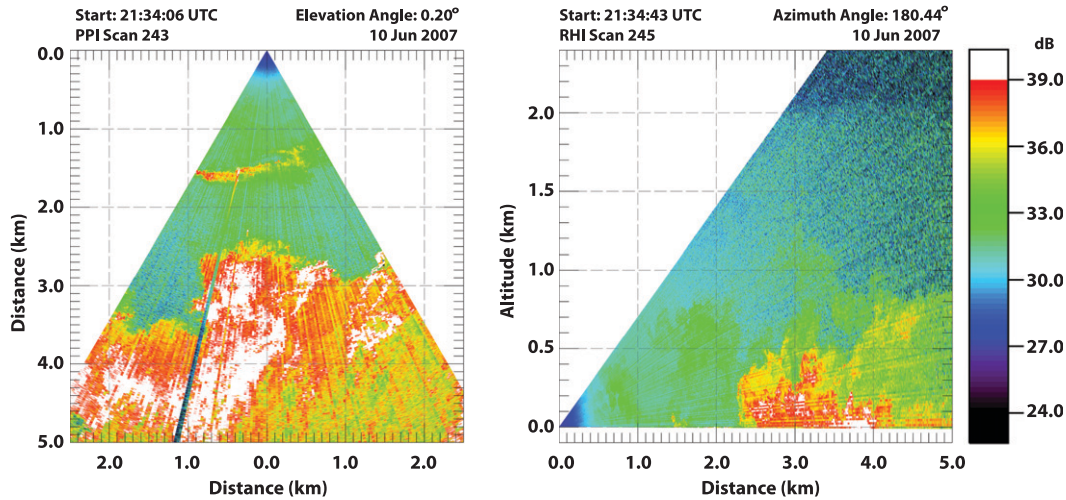
FIG. 11. (left) PPI and (right) RHI scans from 10 Jun 2007. Note the vertical axis in (right) is expanded by a factor of 2 relative to the horizontal axis.

site. The 26 April case shows more of a steplike change while the 1 May case shows a steadily increasing trend. The 14 and 28 May cases show relatively small increases after front passage.

a. Speed of fronts

The simultaneous scanning lidar and in situ observations provide an opportunity to test an equation that relates front speed V_{front} to the change in air density, depth of the denser air mass H, and the speed of the opposing wind component in the air mass ahead of the front V_{wind}. The relationship, based on von Kármán's equation (Karman 1940; Simpson and Britter 1980), is

$$V_{front} = c\sqrt{\frac{\rho_{m2} - \rho_{m1}}{\rho_{m1}}gH} - 0.62V_{wind}, \qquad (1)$$

where c is the internal Froude number, ρ_{m1} is the moist air density of the lighter air mass, ρ_{m2} is the moist air density of the heavier advancing marine air mass, and g is the acceleration due to gravity. The internal Froude number can range from 0.7 to 1.08 and a value of 0.75 was used here (Wakimoto 1982). Table 3 lists the six cases for which in situ data are available, the variables for each case, and the results. Since it was not possible to estimate any case-to-case variation in the depths H of the denser air masses from the lidar scans, a value of 250 m was used for all cases [explained in section 3b(1) below]. The range of the theoretical values matches the range of the observed values, but correlation is not apparent.

More representative measurements may be required to capture the case-to-case variations in front speed. In

this work, changes in the 30-min moist air density were used. Choosing values from different times or averaged over different periods may yield better results. Also, the ability to sense variations in the depth of the density currents and use of an opposing wind speed that is representative of the average over the depth of the outer mixed layer before arrival of the front are likely to help. In the future, more representative horizontal wind speeds could be obtained by tracking the horizontal movement of aerosol features with the correlation technique as was done previously by Mayor and Eloranta (2001).

b. Structure of fronts

The lidar scans provide an ideal opportunity to observe the horizontal and vertical shape of the fronts, and the motion and evolution of coherent structures associated with the fronts. Several articles describe the anatomy of density current fronts including, for example, Britter and Simpson (1978) and Simpson and Britter (1979).

TABLE 3. Variables used to compute the theoretical northward component of front speed and the observed northward front speeds.

Date	ρ_{m1} (kg m^{-3})	ρ_{m2} (kg m^{-3})	H (m)	V_{wind} (m s^{-1})	Speed of front (m s^{-1}) Theor	Obs
24 Apr	1.192 53	1.195 19	250	−1.36	2.6	3.0
26 Apr	1.161 38	1.165 59	250	1.57	1.3	2.0
1 May	1.161 54	1.165 78	250	0.32	2.4	1.0
14 May	1.155 05	1.155 18	250	0.67	0.8	1.3
28 May	1.149 07	1.149 96	250	0.22	1.2	1.1
10 Jun	1.152 39	1.153 71	250	0.03	1.3	3.8

1) VERTICAL STRUCTURE

The predominant mechanism for mixing in the vertical dimension of a density current front is the Kelvin–Helmholtz (K–H) instability (Simpson 1986; Plant and Keith 2007). The lidar RHI scans reveal features that resemble K–H billows in each of the 7 cases. The images show that billows occur on a variety of spatial scales ranging from hundreds of meters to more than a kilometer. Unfortunately, thermodynamic data at these altitudes was not collected during the experiment and therefore the Richardson number cannot be calculated to confirm whether these are indeed K–H billows as was done for thunderstorm gust fronts by Mueller and Carbone (1987). The RHI scans also show the slope of the front. Figure 12 was created by hand-tracing the top edge of the advancing air masses at the indicated times. A nose (the foremost part of the front above the surface) is observed occasionally in the RHI scans, but is not a persistent feature. The RHI animations suggest the presence of a head region, where billows reach a maximum height. The exact depth of the internal boundary layer behind the head is difficult to identify in the RHI scans due to the vigorous mixing that occurs there. It is noted, however, that the altitude of zero-mean horizontal motion of aerosol structures is substantially lower than the maximum height of the billows in this posthead region and, in this work, was used as a value representative of the marine layer depth. For all of these cases, it is estimated to be 250 m AGL.

2) HORIZONTAL STRUCTURE

Instability in a density current front is also manifest in the horizontal dimension by lobe and cleft structure (Simpson 1986; Härtel et al. 2000). Figure 13 shows how the leading edge of the fronts in the atmospheric surface layer progress over time in the horizontal dimension. The contours in Fig. 13 can be compared with those resulting from tank experiments such as Fig. 8 of Simpson (1972) and Fig. 4.1 in Neufeld (2002). The contours from the lidar images show that some of the lobes split over time and some of the clefts fill in. The lidar images, however, do not indicate the presence of sharp clefts that can be seen in the results from tank experiments. This is not likely due to the spatial resolution of the lidar data, but to the nature of the flows. Regions where the lines are crowded in Fig. 13 indicate the front is not advancing in the direction normal to the front. Therefore, the spacing of the lines in Fig. 13 is approximately proportional to the normal component speed of the front. This shows that the forward speed of the front can change substantially over time.

In Fig. 13a, a broad lobe structure advances northward faster than the observed portion of the front located
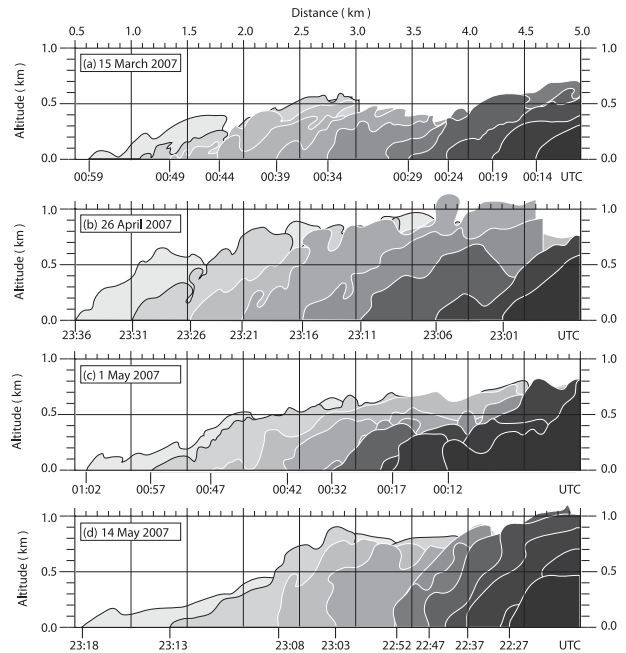

FIG. 12. Position and shape of 4 of the 7 fronts in the RHI scans as hand-traced by an analyst.

west of the meridian that passes through the lidar site and the ISFF VT. In Fig. 13b lobe splitting is observed and it is noted that the speed of the front is generally more steady than in the other cases. In Fig. 13c the lines show the direction of large lobe propagation to the northeast. In Fig. 13d we see that the front is held back initially and then advances rapidly. In Fig. 13e a lobe splits. Finally, in Fig. 13f lobe structures are observed to be moving to the north-northeast.

4. Conclusions

Seven density current fronts were observed on different afternoons over a 3-month period in the spring of 2007 in Dixon, California. In situ data were available for six of the cases. Increases in moist air density across the fronts ranged from 0.0001 to 0.004 kg m^{-3} corresponding to percent difference increases ranging from 0.34% to 0.77% relative to the less dense air mass. The changes in air temperature ranged from $-0.45°$ to $-1.54°$C and increases in water vapor mixing ratios ranged from 1.60 to 2.52 g kg^{-1}. Relative humidities increased between 8% and 15%. The northerly velocity component of the fronts, observed from the lidar time-lapse animations, ranged from 1.0 to 3.8 m s^{-1}. The near-horizontal PPI scans from the lidar revealed lobe and cleft structure of the front while RHI scans revealed vigorous vertical mixing, often resembling K–H billows, and extending up to altitudes between 700 and 1100 m AGL. The lidar
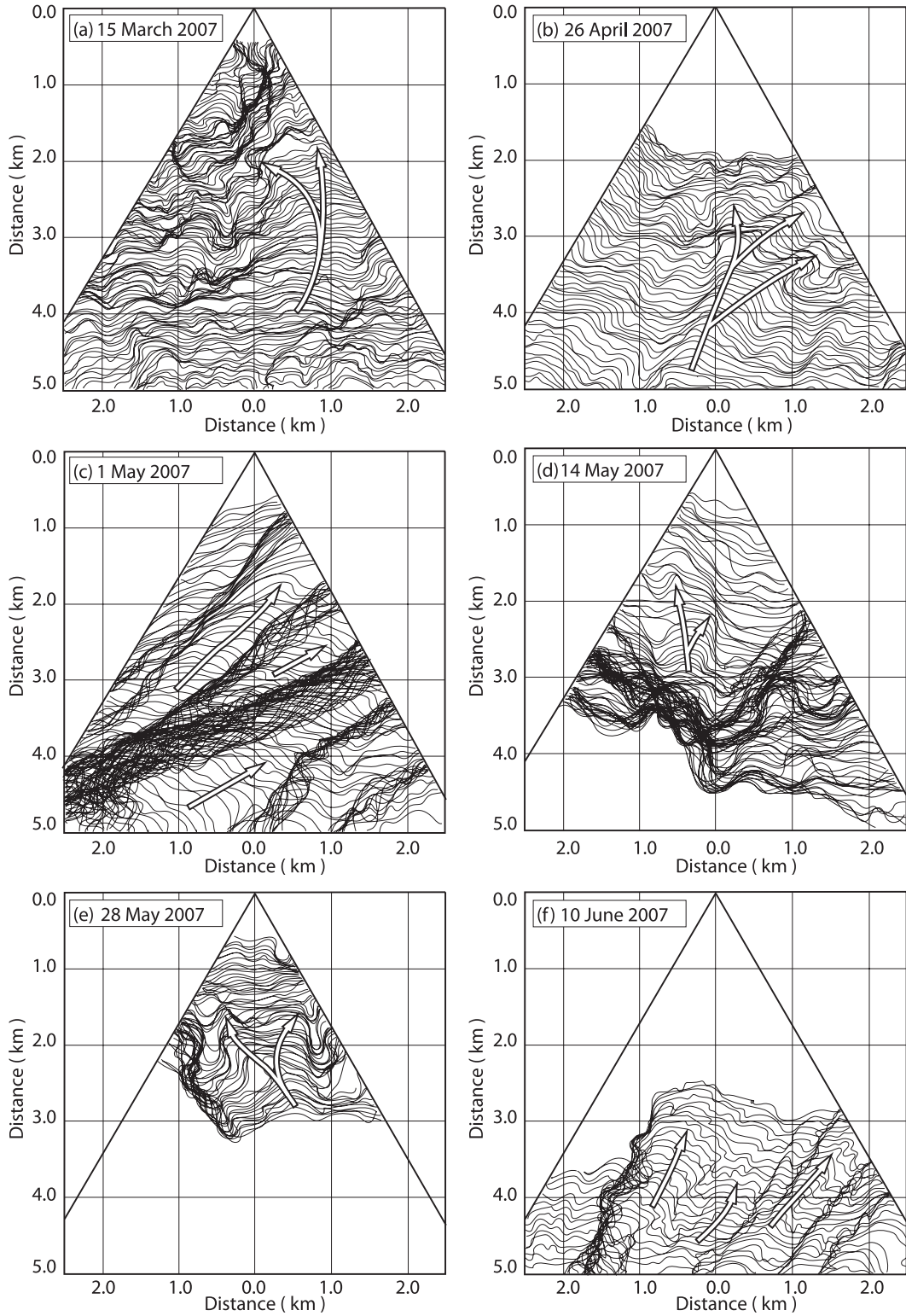
FIG. 13. Position and shape of 6 of the 7 fronts in the PPI scans as hand-traced by an analyst.

data also showed occasional front noses and, in three of the seven cases, strong evidence of wave induced motion in the overlying atmosphere. The depth of the dense air mass behind the front was difficult to ascertain. However, based on the altitude of zero velocity from the average horizontal motion of aerosol features in the RHI scans, it is substantially lower than the peaks of billows near the head. A value of 250 m was used in the calculations of theoretical front speed. In the future, application of algorithms such as wavelets (Davis et al. 2000) and correlation techniques (Mayor and Eloranta 2001) may extract these quantities from the lidar images.

The observations support the hypothesis that the fronts are the leading edges of shallow marine air masses moving north and northeastward from the Sacramento–San Joaquin River Delta region. It is not clear whether the dense air masses have origins from only the Delta region or from the San Francisco Bay or Pacific Ocean. Nor is it clear the cause of the higher backscatter intensity of the denser air mass. It could be the result of an increase in aerosol particle concentration or a similar concentration, but larger size distribution of particles. It is also not clear what role relative humidity and air pollution may play in the increased backscattering. In some of the cases, a part of the increase in aerosol backscatter intensity associated with the front passage may result from the raising of particulate matter from the surface with a sudden increase in the wind speed.

Eye-safety, high single-shot signal-to-noise ratio performance, and multidimensional scanning were required for the lidar to detect and reveal the spatial structure and movement of seven density current fronts. Nearly continuous and unattended observations over a 3-month period enabled excellent temporal sampling and the ability to capture these weak and brief events. The dataset demonstrates the strong synergy of deploying both remote and in situ sensors together. Similar experiments in the future should include the use of aerosol sensors to quantify the relationships between the microphysical properties of particulate matter and changes in backscatter intensity.

Future studies may investigate the synoptic and regional weather conditions in which these fronts form, whether state-of-the-art weather forecast models are capable of resolving and depicting the fronts, and if the fronts have a significant impact on weather forecasts and air quality. Future studies may also investigate changes in surface fluxes, the statistical properties associated with turbulence in the internal boundary layers, and finescale numerical simulation of the cases. Future field experiments could employ a mobile scanning lidar that could move with the fronts to observe them from a Lagrangian perspective. Finally, monitoring the boundary layer in

this location with a scanning lidar and micrometeorological sensor site over long periods of time may result in the discovery of trends in the frequency of occurrence of these fronts. If trends exist, they may be related to changes in land use, synoptic patterns, and climate. Therefore, a multiyear observational effort to monitor the frequency of these fronts may be valuable.

APPENDIX

Calculation of Moist Air Density

Moist air density was calculated as follows. First, saturation vapor pressure was calculated following Bolton (1980):

$$e_s = 6.112 \exp \frac{17.67T}{T + 243.5}, \tag{A1}$$

where T is the temperature in degrees Celsius. Saturation mixing ratio is

$$m_s = \frac{0.622 e_s}{P - e_s}, \tag{A2}$$

where P is the pressure. Water vapor mixing ratio is

$$r = \mathrm{RH} m_s, \tag{A3}$$

where RH is the relative humidity. Dry air density that considers presence of water vapor is

$$\rho_d = P[R_d T(1 + 1.608r)]^{-1}, \tag{A4}$$

where R_d is the dry air gas constant of 287.04 J kg^{-1} K^{-1}. Finally, total air density (both dry and moist parts), and referred to as *moist air density* herein, is

$$\rho_m = \rho_d(1 + r). \tag{A5}$$

REFERENCES

Antonelli, M., and R. Rotunno, 2007: Large-eddy simulation of the onset of the sea breeze. *J. Atmos. Sci.,* **64,** 4445–4457.

Arritt, R. W., 1993: Effects of the large-scale flow on characteristic features of the sea breeze. *J. Appl. Meteor., 32,* 116–125.

Atlas, D., 1960: Radar detection of the sea breeze. *J. Meteor., 17,* 244–258.

Banta, R. M., L. D. Olivier, and D. H. Levinson, 1993: Evolution of the Monterey Bay sea-breeze layer as observed by pulsed Doppler lidar. *J. Atmos. Sci., 50,* 3959–3982.

Benjamin, T. B., 1968: Gravity currents and related phenomena. *J. Fluid Mech., 31,* 209–248.

Bolton, D., 1980: The computation of equivalent potential temperature. *Mon. Wea. Rev., 108,* 1046–1053.

Britter, R. E., and J. E. Simpson, 1978: Experiments on the dynamics of a gravity current head. *J. Fluid Mech., 88,* 223–240.

Cunningham, P., 2007: Idealized numerical simulation of the interaction between buoyant plumes and density currents. *J. Atmos. Sci., 64,* 2105–2115.

Davis, K. J., N. Gamage, C. R. Hagelberg, C. Kiemle, D. H. Lenschow, and P. P. Sullivan, 2000: An objective method for deriving atmospheric structure from airborne lidar observations. *J. Atmos. Oceanic Technol., 17,* 1455–1468.

Eastwood, E., and G. C. Rider, 1961: A radar observation of a sea-breeze front. *Nature, 189,* 978–980.

Härtel, C., F. Carlsson, and M. Thunblom, 2000: Analysis and direct numerical simulation of the flow at a gravity-current head. Part 2. The lobe-and-cleft instability. *J. Fluid Mech., 418,* 213–229.

Hayes, T. P., J. J. R. Kinney, and N. J. M. Wheeler, 1984: California surface wind climatology. Tech. Rep., California Air Resources Board, Sacramento, CA, 180 pp.

Karman, T., 1940: The engineer grapples with nonlinear problems. *Bull. Amer. Math. Soc., 56,* 615–683.

Kolev, I., O. Parvanov, B. Kaprielov, E. Donev, and D. Ivanov, 1998: Lidar observations of sea-breeze and land-breeze aerosol structure on the Black Sea. *J. Appl. Meteor., 37,* 982–995.

Lapworth, A., 2000: Observations of atmospheric density currents using a tethered balloon-borne turbulence probe system. *Quart. J. Roy. Meteor. Soc., 126,* 2811–2850.

Linden, P. F., and J. E. Simpson, 1986: Gravity-driven flows in a turbulent fluid. *J. Fluid Mech., 172,* 481–497.

Mass, C. F., W. J. Steenburgh, and D. M. Schultz, 1991: Diurnal surface-pressure variations over the continental United States and the influence of sea level reduction. *Mon. Wea. Rev., 119,* 2814–2830.

Mayor, S. D., and E. W. Eloranta, 2001: Two-dimensional vector wind fields from volume imaging lidar data. *J. Appl. Meteor., 40,* 1331–1346.

——, S. M. Spuler, B. M. Morley, and E. Loew, 2007: Polarization lidar at 1.54 μm and observations of plumes from aerosol generators. *Opt. Eng., 46,* 096201, doi:10.1117/12.781.

Miller, S. T. K., B. D. Keim, R. W. Talbot, and H. Mao, 2003: Sea breeze: Structure, forecasting, and impacts. *Rev. Geophys., 41,* 1.1–1.31.

Mueller, C. K., and R. E. Carbone, 1987: Dynamics of a thunderstorm outflow. *J. Atmos. Sci., 44,* 1879–1898.

Nakane, H., and Y. Sasano, 1986: Structure of a sea-breeze front revealed by scanning lidar observation. *J. Meteor. Soc. Japan, 64,* 787–792.

Neufeld, J., 2002: Lobe-cleft patterns in the leading edge of a gravity current. M.S. thesis, Dept. of Physics, University of Toronto, 47 pp.

Patton, E. G., and Coauthors, 2011: Canopy Horizontal Array Turbulence Study (CHATS). *Bull. Amer. Meteor. Soc.,* in press.

Pearson, R. A., 1973: Properties of the sea breeze front as shown by a numerical model. *J. Atmos. Sci., 30,* 1050–1060.

Plant, R. S., and G. J. Keith, 2007: Occurrence of Kelvin–Helmboltz billows in sea-breeze circulations. *Bound.-Layer Meteor., 122,* 1–15.

Seitter, K. L., 1986: A numerical study of atmospheric density current motion including the effects of condensation. *J. Atmos. Sci., 43,* 3068–3076.

Simpson, J. E., 1972: Effects of the lower boundary on the head of a gravity current. *J. Fluid Mech., 53,* 759–768.

——, 1986: Mixing at the front of a gravity current. *Acta Mech., 63,* 245–253.

——, 1994: *Sea Breeze and Local Winds.* Cambridge University Press, 252 pp.

——, 1997: *Gravity Currents: In the Environment and the Laboratory.* Cambridge University Press, 244 pp.

——, and R. E. Britter, 1979: The dynamics of the head of a gravity current advancing over a horizontal surface. *J. Fluid Mech., 94,* 477–495.

——, and ——, 1980: A laboratory model of an atmospheric mesofront. *Quart. J. Roy. Meteor. Soc., 106,* 485–500.

——, D. A. Mansfield, and J. R. Milford, 1977: Inland penetration of sea-breeze fronts. *Quart. J. Roy. Meteor. Soc., 103,* 47–76.

Wakimoto, R. M., 1982: The life cycle of thunderstorm gust fronts as viewed with Doppler radar and rawinsonde data. *Mon. Wea. Rev., 110,* 1060–1082.

Wood, R., I. M. Stromberg, and P. R. Jonas, 1999: Aircraft observations of sea-breeze frontal structure. *Quart. J. Roy. Meteor. Soc., 125,* 1959–1995.

Zaremba, L. L., and J. J. Carroll, 1999: Summer wind flow regimes over the Sacramento valley. *J. Appl. Meteor., 38,* 1463–1473.